Research Article

Evaluation of the Modal Coupling Effect in Midstory Isolation Systems Based on Random Vibration Analysis

Xiao Song [1] **and Songtao Xue**[2,3]

[1]*College of Civil Engineering and Architecture, Henan University, Kaifeng, China*
[2]*Department of Architecture, Tohoku Institute of Technology, Sendai, Japan*
[3]*Department of Disaster Mitigation for Structures, Tongji University, Shanghai, China*

Correspondence should be addressed to Xiao Song; songxiao@henu.edu.cn

At present, the midstory isolation (MSI) technology has great potential for application in historical buildings' retrofitting and multifunction buildings. The coupling effect due to the variability of the location of the isolation layer may amplify the structural seismic response and is required for in-depth analysis. This paper aims to evaluate the magnitude of the coupling effect and delimitate the region of the coupling effect to be considered. Based on the complex mode superposition method, the explicit formulas for calculating the random response of the simplified model are deduced. The root-mean-square (RMS) ratio of the shear force coefficient of the upper isolation system is adopted as the performance indicator to evaluate the coupling amplification effect of the MSI system. Parameter analysis indicates that the coupling region is closely related to the mass ratio and frequency ratio of the upper and lower structures to the isolation layer. In general, the region of the coupling effect to be considered can be divided into two parts according to parameters of frequency ratios, depending on the thresholds of the performance indicator. As the mass ratio of the upper isolation system to the entire system increases, one of the coupling regions shrinks and eventually disappears, indicating that the coupling amplification effect in this region can be neglected under certain conditions. Finally, the time-domain analysis of three representative numerical cases of MSI buildings was performed to verify the reliability of the results obtained from the frequency-domain analysis. The research results can provide technical guidance for the preliminary design of the MSI buildings.

1. Introduction

The midstory isolation (MSI) technology is an extension of the base isolation technology and is proved to be effective in reducing seismic response [1–4]. The location of the isolation layer in MSI systems is not restricted. Collisions between the isolation layer and moat walls can be therefore avoided. As the demand for maintenance of existing buildings increased, seismic isolation technology was applied to the reinforcement and renovation of existing buildings, which has contributed to the development of the MSI technology. Training Centers of Taisei Corporation, completed in 1997 [5], were reported as the first applications of retrofit with seismic midisolation method in Japan.

Following this, the MSI technology began to be applied to high-rise multifunctional buildings; typical cases are 63 m Iidabashi First Building [6, 7], 120 m Shiodome Sumitomo Building [8, 9], 200 m Nakanoshima Festival Tower [10], and 230 m Roppongi Grand Tower [11]. By installing the upper seismic isolation system on the top of the existing buildings, the MSI technology is proved to be an effective strategy for adding the new function to existing buildings [12–15]. By inserting the isolation devices into the existing buildings, MSI technology has also been reported for the reinforcement of historic structures in accordance with the current design criteria [16]. Kim and Kang [17] installed magneto-rheological (MR) dampers into the MSI system, which proved to be capable of reducing the displacement demand

of the MSI system. Zhang et al. [18] incorporated the inerter system into the MSI system and verified its effectiveness in reducing the seismic response of the upper substructure and the deformation of the isolation layer. The relevant recent studies reported in [19–24] indicated that the incorporation of negative stiffness elements in isolation devices can also improve the seismic performance of isolated structural systems. In addition, a series of comprehensive studies on the optimal design of MSI systems have been conducted and reported in [25–29]. At present, due to its advantages in construction efficiency and adaptability to diverse needs, MSI technology has great potential for application in retrofitting and the reinforcement of historical buildings as well as in multifunctional buildings.

An MSI building consists of three segments: the lower structure, the isolation layer, and the upper structure. Due to the flexibility of the isolation layer, it was reported that the contribution of higher modes cannot be neglected, and the frequency of predominate modes may not be well separated, which in turn has an impact on the seismic response of the structure, defined as the modal coupling effect. Over the last few decades, a great deal of effort has been documented. Kobayashi et al. [30, 31] carried out a series of eigenvalue analyses and found that the response amplification on the upper structure of the isolated story was caused by modal coupling between modes of vibration on the upper and lower structures. Afterward, Wang et al. [32, 33] extended the validity of Kobayashi et al. [30, 31] methodology, adopting a 3DOF model to investigate the dynamic behavior of MSI structures. Results disclosed that seismic responses at the upper structure were enlarged due to the closeness of the two higher modal frequencies. A linear relationship between the frequency ratios of the upper and lower structures was put forward to predict the condition in which the modal coupling effect occurs. Based on the pole allocation method, Ikeda [34] proposed a closed-form expression to illustrate the tradeoff relationship between the damping ratios of the lower and upper substructures. Faiella and Mele [35, 36] utilized lumped mass multidegree-of-freedom models to identify the range of different behavioral modes and further verified that the modal coupling arises when the higher frequency of the upper structure is close to any frequency of the lower structure.

In the above studies related to the modal coupling effect, researchers mainly focused on the conditions in which modal coupling occurs and qualitatively illustrated the coupling amplification effect by comparing the peak transfer function or seismic response of the upper structure. Little

has been documented for the magnitude of the modal coupling effect and the extent of its influence on the dynamic response of the structure, as well as the relationship between the modal coupling effect and the parameters of segments. Distinct from previous studies, this paper aims to evaluate the magnitude of the modal coupling effect with various design parameters and delimitate the region whether modal coupling should be considered based on the threshold values of performance indicator, which is essential for practical design. The explicit formulas for calculating the random response of the simplified model were derived by the residue theorem. At the same time, a series of dimensionless parameters were introduced for the parametric analysis of structural dynamic response. Then, the RMS ratio of the shear force coefficient of the upper isolation system was adopted as the performance indicator to evaluate the coupling amplification effect of the MSI system. Furthermore, for systems with different design parameters, the region of the modal coupling effect to be considered was delineated according to the performance indicator thresholds. Finally, the time-domain analysis of three representative numerical cases of MSI buildings was performed to verify the reliability of the results obtained from the frequency domain analysis.

2. Thend potential applications, the parameter ran MSI Systems

2.1. Model and Dynamic Equations. To gain insight into the model coupling effect of MSI systems, a simple linear three-degree-of-freedom (3-DOF) model is adopted for elementary analysis with reference to the 2-DOF model adopted in the base isolation system [32, 34, 37]. The MSI system consists of a lower structure, isolation layer, and upper structure, as shown in Figure 1(a). The lower structure can be simplified as an S-DOF system shown in Figure 1(b). With lower structure infinitely rigid, the 3-DOF model of the MSI system degenerates to the 2-DOF model of the base isolation system, as shown in Figure 1(c). The parameters of the models, including mass m, damping c, and stiffness k, are shown in Figure 1, and the subscripts ls, iso, and us denote the lower structure below the isolation layer, the isolation layer, and the upper structure above the isolation layer, respectively.

The dynamic equations of the 3-DOF system subjected to the ground excitation $\ddot{u}_g$ can be expressed as follows:

$$
\begin{aligned}
m_{us}\left(\ddot{x}_{us} + \ddot{x}_{iso} + \ddot{x}_{ls}\right) + m_{iso}\left(\ddot{x}_{iso} + \ddot{x}_{ls}\right) + m_{ls}\ddot{x}_{ls} + c_{ls}\dot{x}_{ls} + k_{ls}x_{ls} &= -(m_{us} + m_{iso} + m_{ls})\ddot{u}_g, \\
m_{us}\left(\ddot{x}_{us} + \ddot{x}_{iso} + \ddot{x}_{ls}\right) + m_{iso}\left(\ddot{x}_{iso} + \ddot{x}_{ls}\right) + c_{iso}\dot{x}_{iso} + k_{iso}x_{iso} &= -(m_{us} + m_{iso})\ddot{u}_g, \\
m_{us}\left(\ddot{x}_{us} + \ddot{x}_{iso} + \ddot{x}_{ls}\right) + c_{us}\dot{x}_{us} + k_{us}x_{us} &= -m_{us}\ddot{u}_g,
\end{aligned}
\tag{1}
$$

where x_{ls}, x_{iso}, and x_{us}, denote the relative displacement of the three masses in 3-DOF. The dot on x_{ls}, x_{iso}, and x_{us} denote

the differential operations with respect to the time t. For simplicity of derivation, the following parameters are defined:
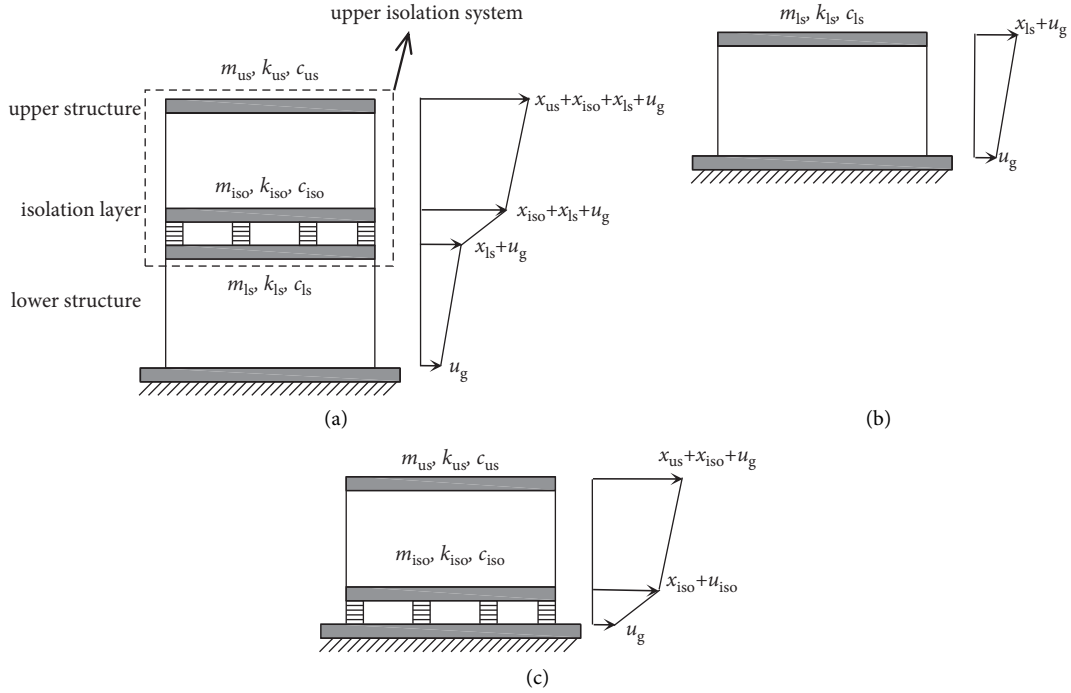
Figure 1: Simplified models for structures with the MSI system and its segment models: (a) 3-DOF model, (b) S-DOF model, and (c) 2-DOF model.

$$r_1 = \frac{m_{iso} + m_{us}}{m_{ls} + m_{iso} + m_{us}},$$

$$r_2 = \frac{m_{us}}{m_{iso} + m_{us}},$$

$$\omega_{ls} = \sqrt{\frac{k_{ls}}{m_{ls}}},$$

$$\omega_{iso} = \sqrt{\frac{k_{iso}}{m_{us} + m_{iso}}},$$

$$\omega_{us} = \sqrt{\frac{k_{us}}{m_{us}}},$$

$$\xi_{ls} = \frac{c_{ls}}{2m_{ls}\omega_{ls}},$$

$$\xi_{iso} = \frac{c_{iso}}{2(m_{iso} + m_{us})\omega_{iso}},$$

$$\xi_{us} = \frac{c_{us}}{2m_{us}\omega_{us}},$$

$$\varepsilon_{ls} = \frac{\omega_{ls}}{\omega_{iso}},$$

$$\varepsilon_{us} = \frac{\omega_{us}}{\omega_{iso}},$$

(2)

where r_1 is the mass ratio of the upper isolation system to the whole system, reflecting the location of the isolation layer in the whole system. r_2 is the mass ratio of the upper structure to the upper isolation system. ξ_{ls} and ξ_{us} are the damping coefficient of the lower structure and the upper structure, respectively, and ξ_{iso} is the equivalent viscous damping ratio

of the upper isolation system. ε_{ls} and ε_{us} are frequency ratios between the different segments.

By introducing the above-defined parameters into equation (1), the dynamic equations for the isolation system can be rewritten as follows:

$$M\ddot{x} + C\dot{x} + Kx = -ME\ddot{u}_g, \quad (3)$$

where M, C, and K are the mass, damping, and stiffness matrices of the system, respectively, and E is the vector that each degree of freedom to the ground motion, and x is the inner-story relative displacement of different segments. The M, C, K, and E matrices related to the 3-DOF system are shown in the following:

$$M = \begin{bmatrix} 1 & r_1 & r_1r_2 \\ 1 & 1 & r_2 \\ 1 & 1 & 1 \end{bmatrix},$$

$$C = \begin{bmatrix} 2\xi_{ls}\varepsilon_{ls}(1-r_1) & 0 & 0 \\ 0 & 2\xi_{iso} & 0 \\ 0 & 0 & 2\xi_{us}\varepsilon_{us} \end{bmatrix} \cdot \omega_{iso},$$

$$K = \begin{bmatrix} \varepsilon_{ls}^2(1-r_1) & 0 & 0 \\ 0 & 1 & 0 \\ 0 & 0 & \varepsilon_{us}^2 \end{bmatrix} \cdot \omega_{iso}^2, \quad (4)$$

$$E = \begin{bmatrix} 1 \\ 0 \\ 0 \end{bmatrix},$$

$$x = \begin{bmatrix} x_{ls} \\ x_{iso} \\ x_{us} \end{bmatrix}.$$

Similarly, for the 2-DOF system and S-DOF system, the dynamic equations can also be written in the form of equation (3). The related matrices for the 2-DOF system are expressed as follows:

$$M = \begin{bmatrix} 1 & r_2 \\ 1 & 1 \end{bmatrix},$$

$$C = \begin{bmatrix} 2\xi_{iso} & 0 \\ 0 & 2\xi_{us}\varepsilon_{us} \end{bmatrix} \cdot \omega_{iso},$$

$$K = \begin{bmatrix} 1 & 0 \\ 0 & \varepsilon_{us}^2 \end{bmatrix} \cdot \omega_{iso}^2, \tag{5}$$

$$E = \begin{bmatrix} 1 \\ 0 \end{bmatrix},$$

$$x = \begin{bmatrix} x_{iso} \\ x_{us} \end{bmatrix},$$

and for the S-DOF system,

$$M = 1,$$

$$C = 2\xi_{ls}\varepsilon_{ls} \cdot \omega_{iso},$$

$$K = \varepsilon_{ls}^2 \cdot \omega_{iso}^2, \tag{6}$$

$$E = 1,$$

$$x = x_{ls}.$$

According to the above analysis, the relevant parameters of the structural dynamic equation (3) are the nondimensional parameters ε_{ls}, ε_{us}, r_1, and r_2; the damping ratios ξ_{ls}, ξ_{iso}, and ξ_{us}; and the frequency of upper isolation system ω_{iso}. Accordingly, the dynamic characteristics and response of the system can be expressed as functions of the above parameters. The damping ratio of the upper and lower structure is generally a given constant that varies with the type of structure. To cover the range of practical applications [5–10, 36] and potential applications, the parameter ranges for related variables are defined as follows:

$$1.5 < \varepsilon_{ls}, \varepsilon_{us} < 15, \ 0.2 < r_1 < 0.9, \ 0.5 < r_2 0.9, \ 0.10 < \xi_{iso} < 0.35. \tag{7}$$

2.2. Dynamic Characteristics. Dynamic characteristics of 3-DOF MSI systems are discussed in this section. The frequencies of the 3-DOF systems are defined as ω_1, ω_2, and ω_3, and the modal participating mass ratios are defined as L_1, L_2, and L_3. According to the basic theory of dynamics, the i-th ($i = 1, 2, 3$) modal participating mass ratios can be calculated as follows:

$$L_i = \frac{\left(\phi_i^T M_m E\right)^2}{\phi_i^T M_m \phi_i}, \tag{8}$$

where $M_m = \text{diag}(1, r_1, r_1 r_2) \cdot M$, M and E can be obtained with equation (4), and ϕ_i is the i-th mode shape of the 3-DOF system.

Figures 2(a)–2(c) summarize the ratios of the fundamental frequencies to the upper isolation system and ratios of adjacent mode frequencies, denoted as ω_1/ω_{iso}, ω_1/ω_2, and

ω_2/ω_3, respectively. From Figure 2(a), it can be seen that the frequency ratio ω_1/ω_{iso} increases with the increase of the frequency ratio ε_{ls}, and ε_{us}. The first natural frequency of the 3-DOF model is close to the first natural frequency of the upper isolation system. As shown in Figure 2(b), with the increase of ε_{ls}, the frequency ratio ω_1/ω_2 decreases after the increase in the first time and then tends to stabilize. The maximum value of ω_1/ω_2 is about 0.3, which validates the first and second frequencies are far apart. On contrary, as shown in Figure 2(c), it is apparent that values on the peak line of ω_2/ω_3 vary in a very narrow range with values close to 1, indicating that the modal coupling occurs between the second and third modes. Further numerical analysis shows that the frequency ratio corresponding to the peak line of ω_2/ω_3 satisfies the following relationship:

$$\varepsilon_{us} = \varepsilon_{ls} \sqrt{1 - r_2}, \tag{9}$$

which is proved to be consistent with the equation proposed in [32]. Interestingly, based on Kelly's work [37], for the 2-DOF system shown in Figure 1(b), the approximation of second frequency is given by

$$\omega_2^{II} = \frac{\omega_{us}}{\sqrt{1 - r_2}}. \tag{10}$$

On the other hand, for the S-DOF system shown in Figure 1(c), we have

$$\omega_1^{I} = \omega_{ls}. \tag{11}$$

Comparing equations (9)–(11), it can be concluded that the model coupling occurs when the second frequency of the upper isolation system is close to the first frequency of the lower structure, which is similar to the tuning effect of TMD.

Substituting equation (9) into equation (3), the second frequency of the 3-DOF system can be obtained as $\omega_2 = \omega_{ls}$, and the modal shape vectors can be expressed as $[1 \ 0 \ -1/r_2]^T$. Correspondingly, the second modal participating mass ratio defined in equation (8) can be calculated as follows:

$$L_2 = \frac{(1 - r_1)^2}{r_1 (1/r_2 - 1) + (1 - r_1)}. \tag{12}$$

Accordingly, the modal participating mass ratios L_1 and L_3 can be approximated as follows:

$$L_1 = 1 - L_2, \tag{13}$$
$$L_3 = 0.$$

As indicated in equation (12), it is apparent that L_2 increases smoothly with increasing mass ratio r_2 and decreases with increasing mass ratio r_1. Moreover, the above analysis clearly shows that when modal coupling occurs, the vibration of the structure is characterized by the first and the second modal vibration, where the second modal participating mass ratio affects the magnitude of the coupling effect. When coupling occurs, the larger the L_2, the more significant the coupling effect. As shown above, equations (12) and (13) are calculated with the condition of equation (9); it is worthwhile to investigate the influence of related parameters on the modal participating mass ratios under general conditions.
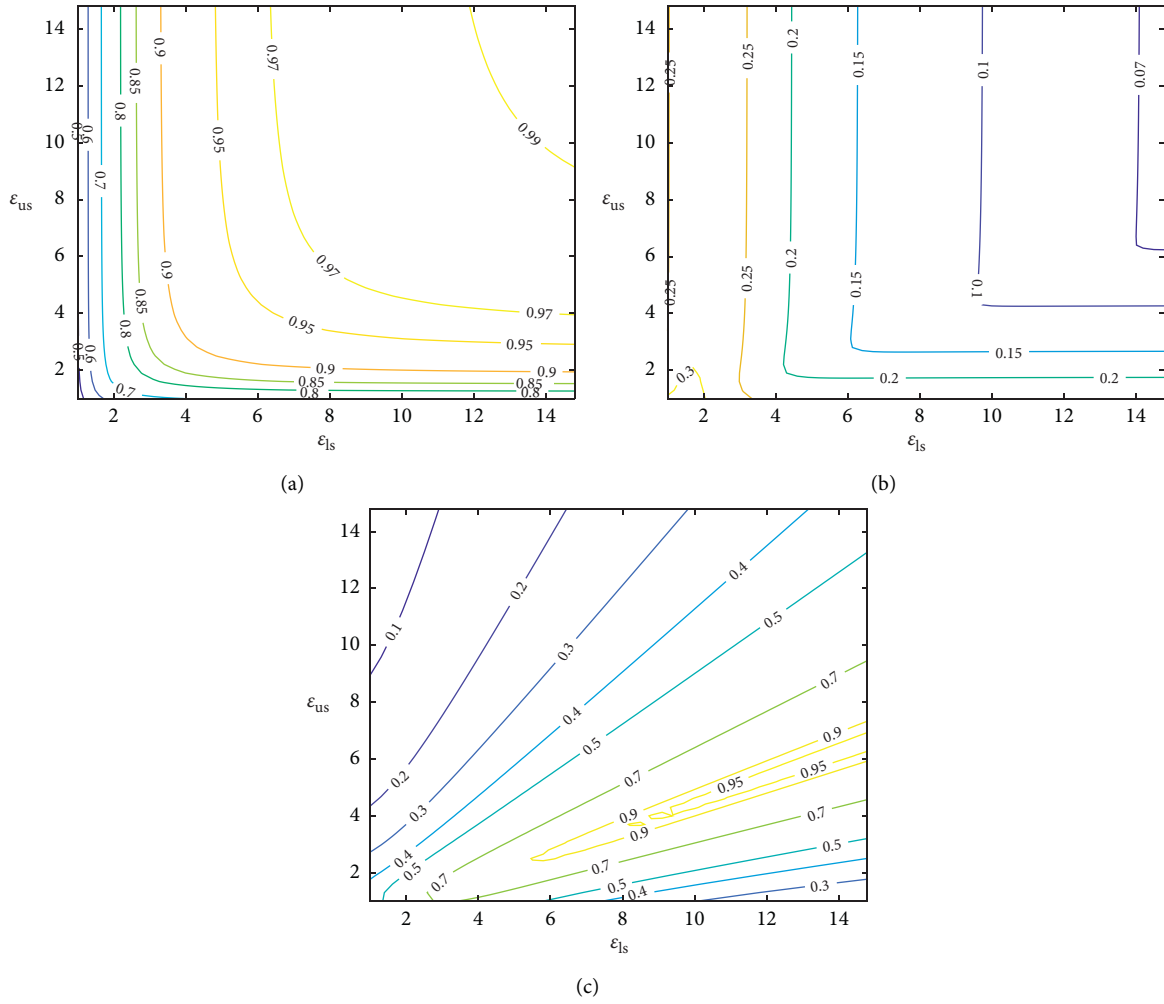
(a)

(b)

(c)

FIGURE 2: Mode frequency ratios with various ε_{ls} and ε_{us} ($r_1 = 0.7$ and $r_2 = 0.8$): (a) ω_1/ω_{iso}, (b) ω_1/ω_2, and (c) ω_2/ω_3.

The modal analysis indicates that the first mode of the 3-DOF is characterized as the first-order vibration of the upper isolation system, and the second and third orders are characterized as the second mode of the upper isolation system or the first mode of the lower structure, depending on the value of the frequency ratio. The variation of modal participating mass ratios also reflects the transition of the dominant modes. Figure 3 presents the comparison of the modal participating mass ratios L_1, L_2, and L_3 corresponding to the variation of the mass ratios r_1 and r_2 and the frequency ratio ε_{ls}, when the frequency ratio $\varepsilon_{us} = 4$, for example. As depicted in Figure 3(a), it can be seen that the first modal participating mass ratio L_1 may be significantly affected by the mass ratio r_1. The increase in r_1 resulted in the increase of L_1, and L_1 gradually decreases and approaches r_1 with the increase of the frequency ratio ε_{ls}. As for L_2 and L_3, it is apparent that at $\varepsilon_{ls} = 8.95$, the effective mode switches from the second to the third mode. Moreover, $L_2 + L_3$ increases slightly and approaches to $(1 - r_1)$ as ε_{ls} increases. It is reasonable to assume that the mass ratio r_1 plays an important role in the dynamic response of the MSI system.

As shown in Figure 3(b), the first modal participating mass ratio L_1 remains stable as r_2 varies. From the comparison of L_2

and L_3 in Figure 3(b), it can be seen that r_2 has a great influence on the values corresponding to the switching points. The frequency ratios ε_{ls} for the effective modal switching point are 5.65, 7.30, and 12.65, corresponding to r_2 of 0.5, 0.7, and 0.9, respectively. In summary, it should be noted that both mass ratios r_1 and r_2 have an evident influence on modal participating mass ratios: r_1 affects the stable value of the first mode, while r_2 affects the position of the switching point between the second and third modes. The application of the MSI technique causes the fundamental change in the basic dynamic characteristics of the system.

3. Modal Coupling Effect of MSI Systems

3.1. The Absolute Acceleration Response of n-DOF (n = 1, 2, and 3) Systems. The MSI technique protects the upper structure by mitigating the vibration induced by the lower structure. Meanwhile, the vibration of the lower structure decreases with the building mass damper effect induced by the upper isolation system. The vibration mitigating effect can be visually reflected in the acceleration of different segments. Therefore, the absolute acceleration is of importance and is therefore analyzed in this study.
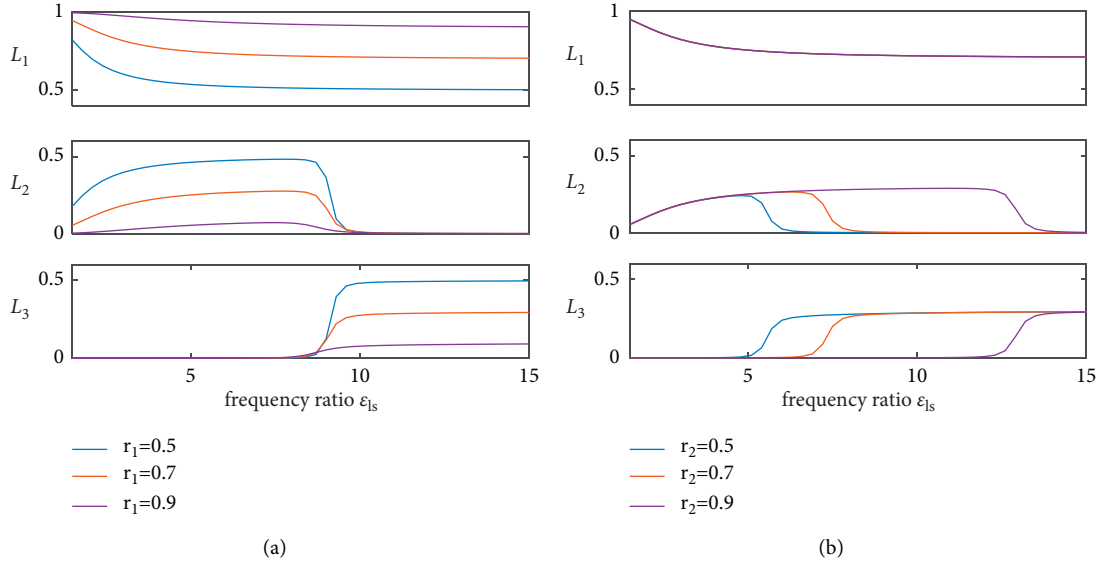
L_1

L_2

L_3

frequency ratio ε_{ls}

— $r_1 = 0.5$
— $r_1 = 0.7$
— $r_1 = 0.9$

(a)

L_1

L_2

L_3

frequency ratio ε_{ls}

— $r_2 = 0.5$
— $r_2 = 0.7$
— $r_2 = 0.9$

(b)

FIGURE 3: Modal participating mass ratios with various ε_{ls} ($\varepsilon_{us} = 4$): (a) $r_2 = 0.8$ and (b) $r_1 = 0.7$.

Substituting the base acceleration $\ddot{u}_g = U_0 e^{i\omega t}$ in equation (3), the absolute acceleration transfer function of all masses in the n-DOF ($n = 1, 2, 3$) systems can be derived from equation (3). Moreover, according to the integral formula for random vibration analysis [38], the variance of acceleration response σ^2 of the n-DOF system under white-noise random excitation (with the constant power spectral density S_0), can be described as follows:

$$\sigma^2 = \int_{-\infty}^{\infty} |H(\omega)|^2 d\omega = \omega_{iso} \cdot S_0 \int_{-\infty}^{\infty} \frac{\Xi_m(\varepsilon)}{\Lambda_m(i\varepsilon)\Lambda_m(-i\varepsilon)} d\varepsilon,$$

(14)

where

$$\Xi_m(\varepsilon) = B_{m-1}\varepsilon^{2m-2} + B_{m-2}\varepsilon^{2m-4} + \cdots + B_0,$$
$$\Lambda_m(i\varepsilon) = A_m(i\varepsilon)^m + A_{m-1}(i\varepsilon)^{m-1} + \cdots + A_0.$$

(15)

$H(\omega)$ is the frequency response function of the absolute acceleration for different segments, which can be calculated according to Laplace transformation of equation (3). ε is given by $\varepsilon = \omega/\omega_{iso}$, which represents the frequency ratios of excitation to the upper isolation system. B_0-B_{m-1} and A_0-A_m are time-invariant real constants. Taking absolute acceleration of the upper mass in the 3-DOF model as an example, B_0-B_{m-1} and A_0-A_m are given as follows:

$$B_0 = \varepsilon_{ls}^4 \varepsilon_{us}^4 (1 - r_1)^2,$$
$$B_1 = 4\varepsilon_{ls}^2 \varepsilon_{us}^2 (1 - r_1)^2 (\xi_{ls}^2 \varepsilon_{us}^2 + \xi_{iso}^2 \varepsilon_{ls}^2 \varepsilon_{us}^2 + \xi_{us}^2 \varepsilon_{ls}^2),$$
$$B_2 = 16\varepsilon_{ls}^2 \varepsilon_{us}^2 (1 - r_1)^2 \left[\xi_{iso}^2 (\xi_{ls}^2 \varepsilon_{us}^2 + \xi_{us}^2 \varepsilon_{ls}^2) + \xi_{ls}^2 \xi_{us}^2 \right],$$
$$B_3 = 64\xi_{ls}^2 \xi_{iso}^2 \xi_{us}^2 \varepsilon_{ls}^2 \varepsilon_{us}^2 (1 - r_1)^2,$$
$$B_4 = B_5 = 0.$$

(16)

$$A_0 = \varepsilon_{ls}^2 \varepsilon_{us}^2 (1 - r_1),$$
$$A_1 = 2\varepsilon_{ls}\varepsilon_{us} (\xi_{ls}\varepsilon_{us} + \xi_{us}\varepsilon_{ls} + \xi_{iso}\varepsilon_{ls}\varepsilon_{us})(1 - r_1),$$
$$A_2 = \left[\varepsilon_{ls}^2 (1 + \varepsilon_{us}^2) + 4\varepsilon_{ls}\varepsilon_{us} (\xi_{ls}\xi_{us} + \xi_{ls}\xi_{iso}\varepsilon_{us} + \xi_{iso}\xi_{us}\varepsilon_{ls}) \right] (1 - r_1) + \varepsilon_{us}^2,$$
$$A_3 = 2\varepsilon_{ls} (1 - r_1)(\xi_{ls}\varepsilon_{us}^2 + \xi_{us}\varepsilon_{ls}\varepsilon_{us} + \xi_{ls} + \xi_{iso}\varepsilon_{ls} + 4\xi_{ls}\xi_{us}\xi_{iso}\varepsilon_{us}) + 2\varepsilon_{us} (\xi_{us} + \xi_{iso}\varepsilon_{us}),$$
$$A_4 = (1 - r_1)(\varepsilon_{ls}^2 (1 - r_2) + \varepsilon_{us}^2 + 4\xi_{ls}\xi_{iso}\varepsilon_{ls} + 4\xi_{ls}\xi_{us}\varepsilon_{ls}\varepsilon_{us}) + (1 - r_1 r_2) + 4\xi_{iso}\xi_{us}\varepsilon_{us},$$
$$A_5 = 2 \left[\xi_{ls}\varepsilon_{ls} (1 - r_1)(1 - r_2) + \xi_{us}\varepsilon_{us} (1 - r_1) + \xi_{iso} (1 - r_1 r_2) \right],$$
$$A_6 = (1 - r_1)(1 - r_2).$$

(17)

Substituting equations (16) and (17) in the resultant equations in Appendix, RMS of the absolute acceleration σ for the upper mass in the 3-DOF model can be obtained as

an explicit function of the design parameters r_1, r_2, ε_{ls}, ε_{us}, ξ_{ls}, ξ_{iso}, and ξ_{us}. The calculations required for random vibration analysis can be significantly simplified with equation (14)

and the equations in Appendix. Similar expressions can be obtained for the lower mass and isolation mass in the 3-DOF model and the corresponding mass in 2-DOF and S-DOF models.

3.2. Performance Indicator for the Modal Coupling Effect.

Based on the effectiveness of the n-DOF ($n = 1, 2, 3$) models in capturing the acceleration response for MSI systems, base isolation systems, and fixed-base systems, the coupling amplification effect can be conducted in the frequency domain. In this section, comparisons in the response of the MSI systems and the evaluation of the coupling effect are conducted.

To analyze the absolute acceleration amplification of the lower mass, isolation mass, and upper mass in the 3-DOF model, ratios are defined as follows:

$$Ra_{ls} = \frac{\mathrm{III}\sigma_{ls}}{\mathrm{I}\sigma_{ls}},$$

$$Ra_{iso} = \frac{\mathrm{III}\sigma_{iso}}{\mathrm{II}\sigma_{iso}}, \qquad (18)$$

$$Ra_{us} = \frac{\mathrm{III}\sigma_{us}}{\mathrm{II}\sigma_{us}},$$

where σ is the RMS value of the absolute acceleration response, which can be calculated with equation (14). The subscripts III, II, and I represent 3-DOF, 2-DOF, and S-DOF systems, respectively.

Figures 4(a)–4(c) illustrate the RMS ratios Ra_{ls}, Ra_{iso}, and Ra_{us} of the absolute acceleration with respect to different frequency ratios ε_{ls} and ε_{us} ($r_1 = 0.8$, $r_2 = 0.7$, and $\xi_{iso} = 0.20$). It can be observed that Ra_{ls} for the lower mass varies between 0.3 and 0.8, and Ra_{iso} and Ra_{us} for the isolation mass and upper mass vary between 1.0 and 1.6. This indicates that the response of the lower structure can be significantly reduced compared to the corresponding fixed-base structure with the installation of the upper isolation system. On the contrary, due to the flexibility of the lower structure, the response of the upper isolation system is amplified compared with the base isolation system. Furthermore, it is worth noting that there are apparent peak lines in Figures 4(a)–4(c), and it is verified that the relationship of frequency ratios corresponding to the peak lines is approximately consistent with equation (9).

This study focuses on the modal coupling amplification effect of the MSI system caused by the flexible isolation layer. The above analysis indicates that the absolute acceleration amplification effect occurs in the upper mass and isolation mass. Therefore, the RMS ratio Ra_{ui} is adopted as the performance indicator to analyze the coupling amplification effect, defined as follows:

$$Ra_{ui} = \frac{{}_{III}\sigma_{a_{ui}}}{{}_{II}\sigma_{a_{ui}}}, \qquad (19)$$

where a_{ui} is the shear force coefficient of the upper isolation system, defined as follows:

$$a_{ui} = \frac{m_{iso}\ddot{x}_{iso} + m_{us}\ddot{x}_{us}}{m_{iso} + m_{us}} = (1 - r_2)\ddot{x}_{iso} + r_2\ddot{x}_{us}, \qquad (20)$$

where σ is the RMS of the shear force coefficient, which can be calculated with equations (14) and (20). The subscripts III and II represent 3-DOF and 2-DOF systems, respectively. The design conditions are defined as follows:

$$Ra_{ui} \leq [RA], \qquad (21)$$

where $[RA]$ is the design threshold, which can be determined according to the seismic design performance requirements. To examine the influence of the upper and lower structures on the dynamic performance of the 3-DOF MSI systems, the boundary curve with $[RA] = 1.2$ is adopted for illustration. The contours of variation of Ra_{ui} with frequency ratios ε_{ls} and ε_{us} are plotted in Figures 5 and 6 for $r_2 = 0.7$ and $\xi_{iso} = 0.20$ and $r_2 = 0.9$ and $\xi_{iso} = 0.20$, respectively.

For simplicity thereafter, the regions delineated in Figures 5 and 6 are summarized in Figure 7. According to the given $[RA]$, the relevant parameter range can be divided into four regions A–D, as shown in Figure 7. Specifically, there is a peak line in region C, which is consistent with Figure 5. Regions A and C with amplification factor $Ra_{ui} > [RA]$ are defined as the coupling regions, while regions B and D with $Ra_{ui} < [RA]$ can be defined as design regions. As depicted in Figures 5 and 6, the amplification patterns of regions A and C are completely different. Combined with the dynamic characteristics analysis in Section 2.2, it can be inferred that for region A, the amplification effect is caused by modal coupling between first and second modes, while for region C, it is caused by modal coupling between second and third modes.

As shown in Figure 5, in the four cases, the scope of region A remains stable and can be expressed as $\varepsilon_{ls} < 3$ approximately. The value of Ra_{ui} in region A tends to decrease rapidly with the increase of ε_{ls} and remains essentially constant with ε_{us}. The scope of coupling region C gradually decreases with the mass ratio r_1 varies from 0.2 to 0.7. In particular, when r_1 is 0.8, region C disappears, and regions B and D are combined. This indicates that the coupling amplification effect caused by the coupling between second and third modes is gradually weakening with the increase of mass ratio r_1. In addition, the peak line in region C is approximately parallel to the boundary line of the region and is independent of the frequency of the upper isolation system ω_{iso}. The results show that the seismic response of the upper isolation system can be reduced by slightly adjusting the frequency ratios ε_{ls} and ε_{us} according to the characteristics of different regions.

The comparison of Figures 5(b) and 6(a) shows that as r_2 increases, the scope of region C shrinks rapidly, and the values on the peak line decrease accordingly. As for the case $r_1 = 0.7$ and $r_2 = 0.9$, region C disappears as shown in Figure 6(b), indicating that the coupling effect in region C can be ignored with the increase of both mass ratios r_1 and r_2. In addition, the comparison of the peak line in region C in Figures 5 and 6 reveals that the slope of the peak line decreases with the increase of r_2. Further numerical analysis indicates that the peak line is parallel to the line corresponding to equation (9), which can be expressed as follows:
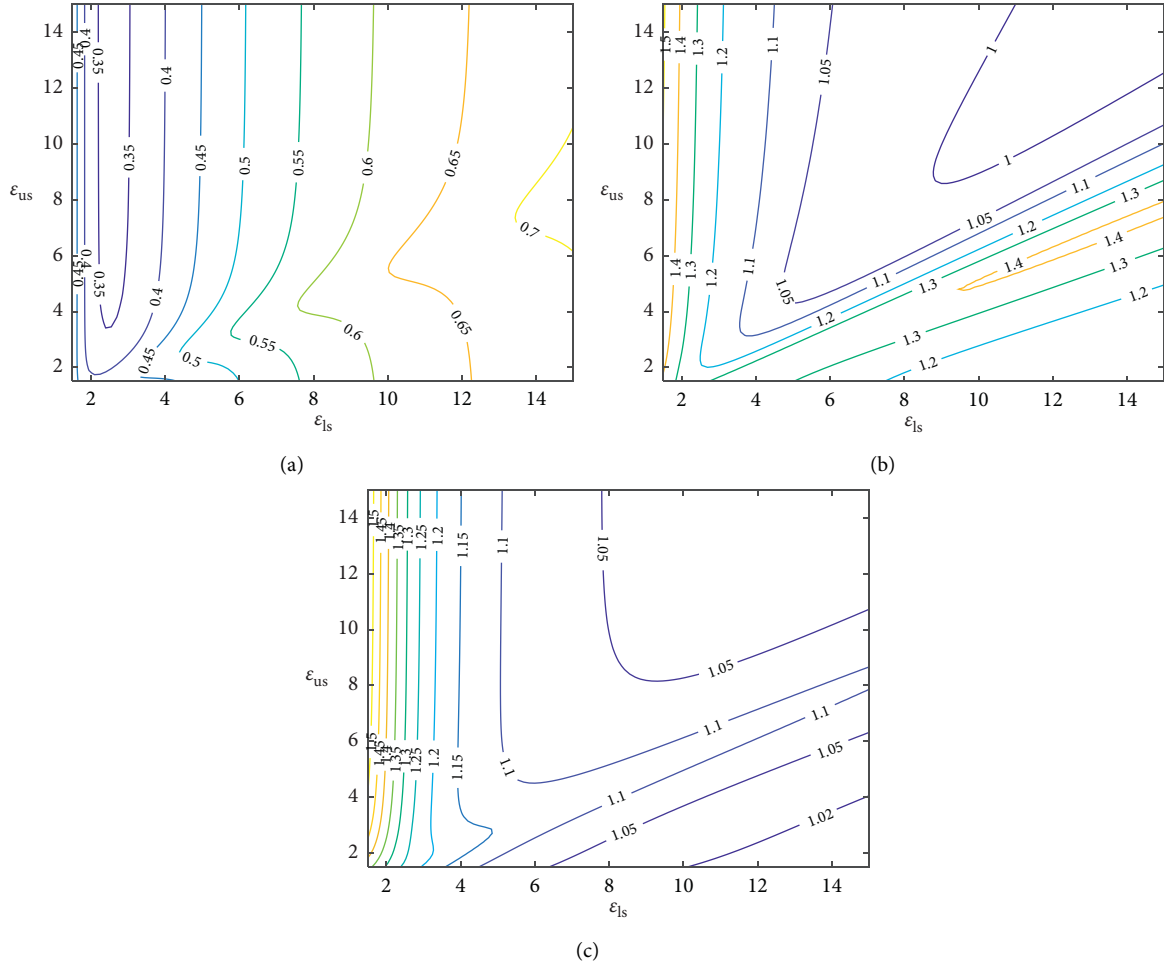
(a)

(b)

(c)

FIGURE 4: Variance ratios of absolute acceleration with various ε_{ls} and ε_{us} ($r_1 = 0.8$ and $r_2 = 0.7$): (a) Ra_{ls} for the lower mass, (b) Ra_{iso} for the isolation mass, and (c) Ra_{us} for the upper mass.

$$\varepsilon_{us} = \varepsilon_{ls}\sqrt{1 - r_2} - d, \tag{22}$$

where d is the deviation between results of the peak line obtained from response analysis of equations (14) and (19) and the peak line of ω_2/ω_3 deduced from eigenvalue analysis. For different cases, the values of d are shown in Table 1. It can be observed that d varies between 0.18 and 0.26 and increases with the increase of r_1 and r_2, indicating that the peak line of Ra_{ui} deviates from the line obtained from the nominal frequency relation, while equation (9) can only approximately predict the peak line.

To investigate the influence of damping ratio ξ_{iso} on the response of the upper isolation system, the variation surface of Ra_{ui} as a function of damping ratio of the upper isolation system ξ_{iso} and the frequency ratio ε_{ls} for $\varepsilon_{us} = 4$ is plotted in Figure 8. It is seen that when ε_{ls} is greater than 5, the ratio Ra_{ui} increases with the increase of damping ratio, which means the decrease of the isolation effect.

Figure 9 shows the contour of the system with $\xi_{iso} = 0.30$ versus the frequency ratios ε_{ls} and ε_{us}. Compared with the system with $\xi_{iso} = 0.20$ shown in Figure 6(b), the slope of the peak line remains the same while the position is shifted upward. Further analysis shows that as the damping ratio ξ_{iso}

increases from 0.2 to 0.3, the value of Ra_{ui} decreases in region A and increases in region C. Correspondingly, the scope of region C increases.

4. Application to Case Buildings

For application, two actual cases, the Iidabashi First Building [9, 36] (denoted as Case 1) and the Shiodome Sumitomo Building [9, 36] (denoted as Case 2), and one calculation case (denoted as Case 3) are selected as cases to investigate the coupling effect of the MSI systems with frequency ratios in different regions. Case 3 is a numerical calculation model of a ten-story building designed so that the structural parameters are located on the peak line of Ra_{ui}. The damping ratios of the upper structure and lower structure ξ_{ls} and ξ_{us} for the three cases are 0.02. The 3-DOF model for MSI structure is utilized, and the related original and calculated parameters for the three cases are shown in Table 2.

4.1. Frequency Response Analysis. The contours of the performance indicator Ra_{ui} derived from the given mass ratios r_1 and r_2 and damping ratio ξ_{iso}, as well as the location of the
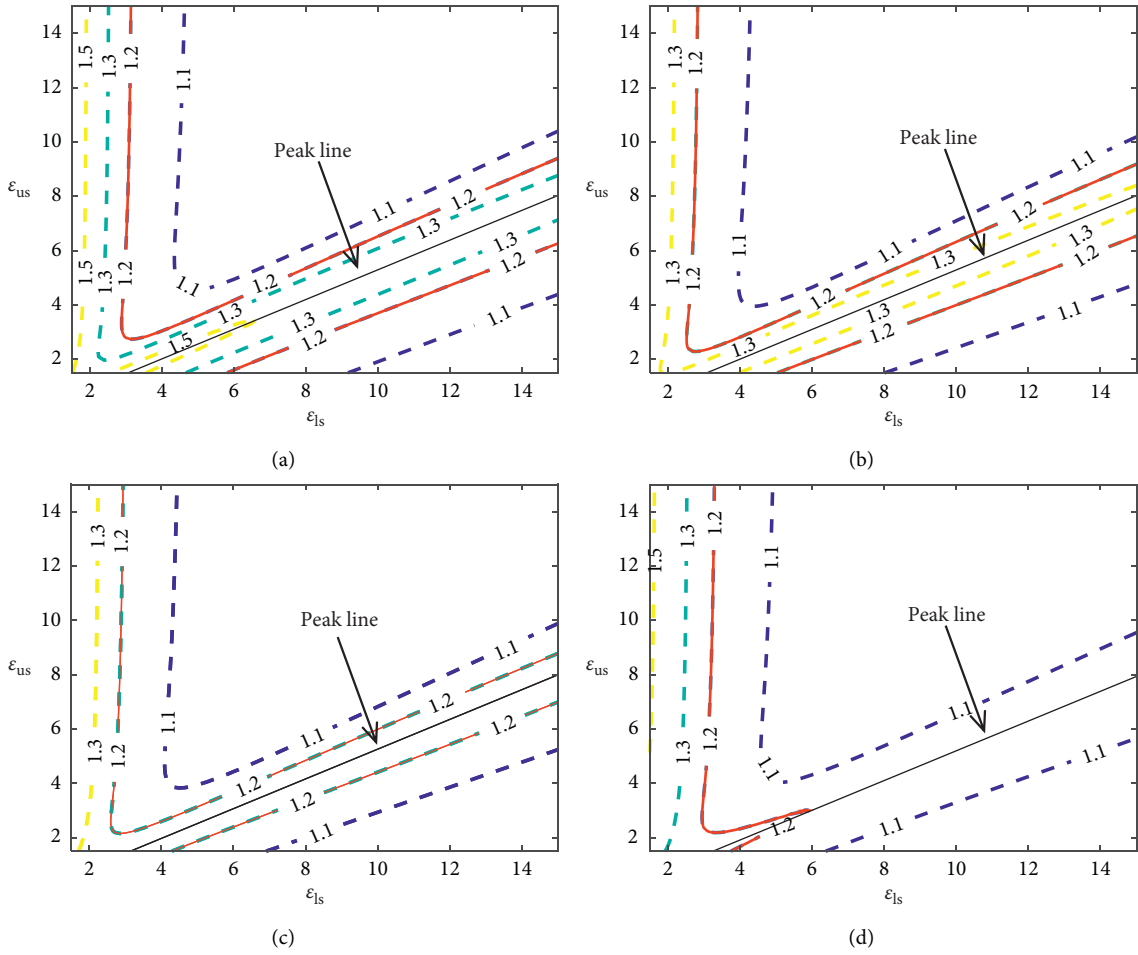
(a)

(b)

(c)

(d)

FIGURE 5: Contour plots of Ra_{ui} with various ε_{ls} and ε_{us}: (a) $r_1 = 0.2$ and $r_2 = 0.7$, (b) $r_1 = 0.5$ and $r_2 = 0.7$, (c) $r_1 = 0.7$ and $r_2 = 0.7$, and (d) $r_1 = 0.8$ and $r_2 = 0.7$.
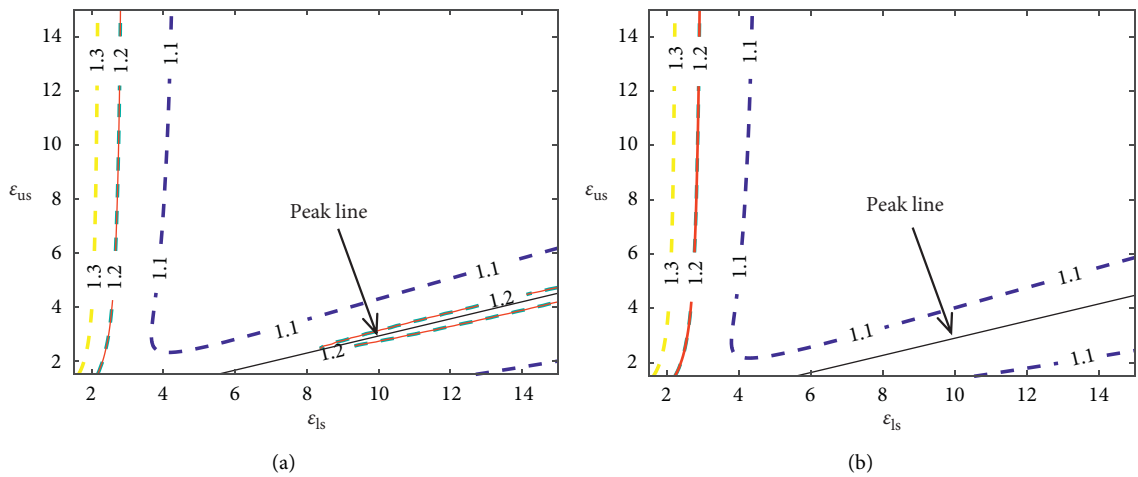

(a)

(b)

FIGURE 6: Contour plots of Ra_{ui} with various ε_{ls} and ε_{us}: (a) $r_1 = 0.5$ and $r_2 = 0.9$ and (b) $r_1 = 0.7$ and $r_2 = 0.9$.

design parameters adopted in practical applications (denoted as E_{ls} and E_{us}, marked by the red circle), are shown in Figures 10–12 for Cases 1–3, respectively. It is seen that the design parameters of Cases 1–3 correspond to different regions of coupling effect. According to the delineation of

the regions in Figure 7, it can be seen that Case 1 is located in the coupling region A, Case 2 in the intersection of regions A and C, and Case 3 on the peak line of the coupling region C.

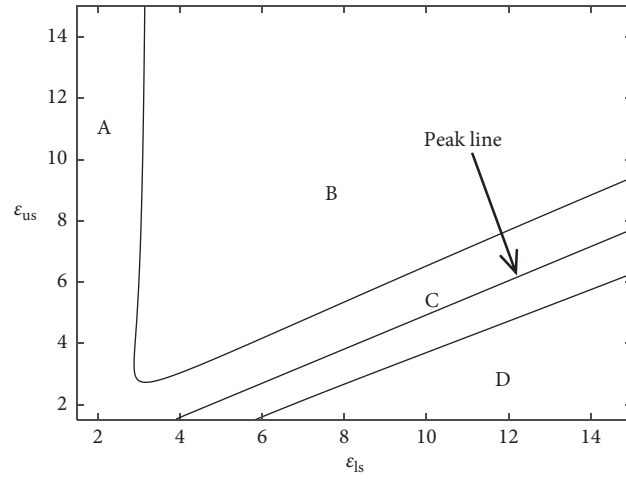Therefore, in order to compare the coupling effect in different regions, the frequency ratio ε_{ls} is selected as the

FIGURE 7: Division of the region of the coupling amplification effect.

TABLE 1: The values of d.

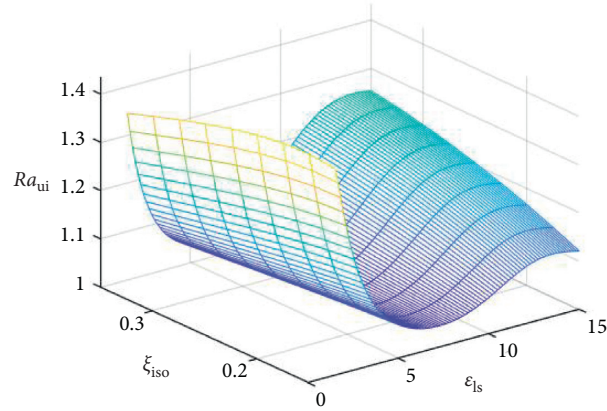| Case	$r_2 = 0.7$				$r_2 = 0.9$	
	$r_1 = 0.2$	$r_1 = 0.5$	$r_1 = 0.7$	$r_1 = 0.8$	$r_1 = 0.5$	$r_1 = 0.7$
d	0.18	0.19	0.22	0.28	0.24	0.26

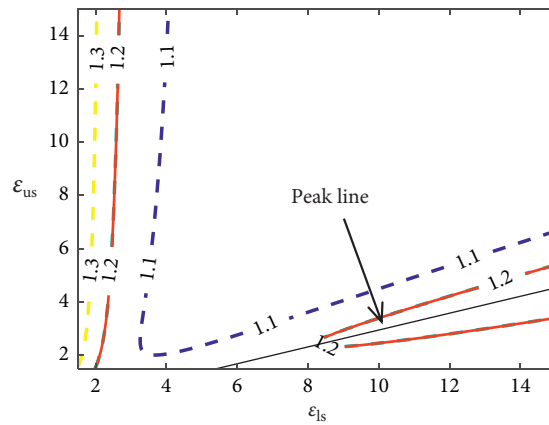FIGURE 8: Contour plot of Ra_{ui} with various ε_{ls} and ξ_{iso} ($r_1 = 0.7$, $r_2 = 0.9$, and $\varepsilon_{us} = 4$).
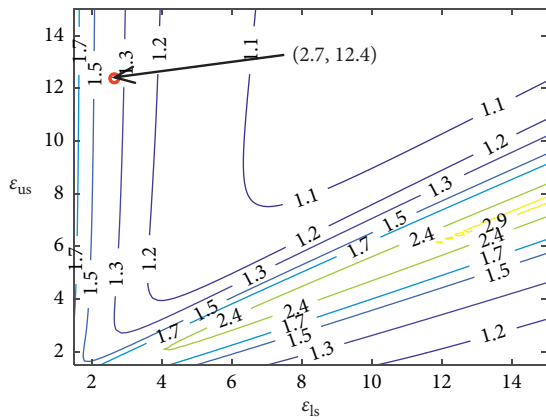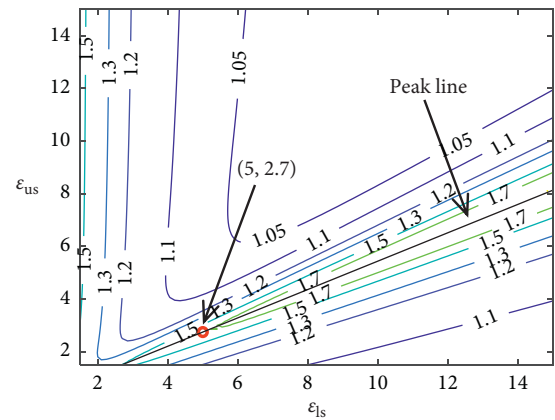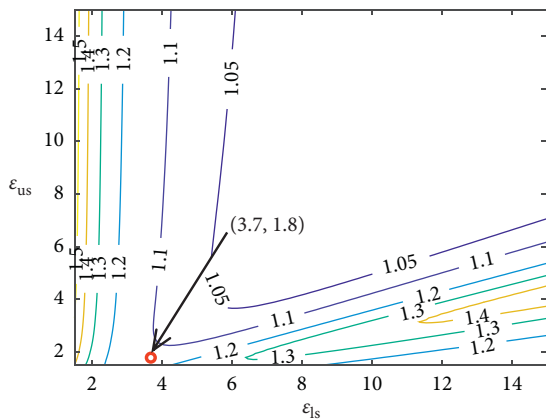

FIGURE 9: Contour plot of Ra_{ui} with various ε_{ls} and ξ_{iso} ($r_1 = 0.7$, $r_2 = 0.9$, and $\xi_{iso} = 0.30$).

TABLE 2: Related parameters for the three cases.

Parameters		Case 1	Case 2	Case 3
Original parameters	m_{ls} (kNs^2/m)	54171	23940	3630
	m_{iso} (kNs^2/m)	4022	4030	2540
	m_{us} (kNs^2/m)	10899	47528	5930
	ξ_{iso}	0.235	0.20	0.20
	T_{ls} (s)	0.98	1.06	0.6
	T_{iso} (s)	2.60	3.90	3.00
	T_{us} (s)	0.21	2.18	1.11
Calculated parameters	r_1	0.22	0.68	0.70
	r_2	0.73	0.92	0.70
	ω_{iso} (rad/s)	2.42	1.61	2.09
	ε_{ls}	2.7	3.7	5.0
	ε_{us}	12.4	1.8	2.7

ω_{iso} and T_{iso} are the frequency and period of the upper isolation system, respectively.

FIGURE 10: Contour plot of Ra_{ui} with various ε_{ls} and ε_{us} (Case 1).

FIGURE 12: Contour plot of Ra_{ui} with various ε_{ls} and ε_{us} (Case 3).

FIGURE 11: Contour plot of Ra_{ui} with various ε_{ls} and ε_{us} (Case 2).

TABLE 3: Variables for comparison.

Case	Variables
Case 1	$(E_{ls}-, E_{ls}, E_{ls}+) = (2.0, 2.7, 3.0)$
Case 2	$(E_{us}-, E_{us}, E_{us}+) = (1.5, 1.8, 2.3)$
Case 3	$(E_{us}-, E_{us}, E_{us}+) = (2.2, 2.7, 3.2)$

variable for Case 1 and the frequency ratio ε_{us} for Cases 2 and 3, as shown in Table 3.

The RMS ratios Ra for the upper mass, the isolation mass, and the lower mass of Case 3 are shown in Figure 13. As depicted, for different segments of the structure, the peak response is located at $\varepsilon_{us} = E_{us}$. It should be noted that in general, the RMS ratios Ra for the upper mass and isolation mass are greater than 1, while Ra for the lower mass are less than 1, and all of them gradually approach 1 as the frequency ratio ε_{ls} increases, indicating that the response of the MSI structure is consistent with that of the base-isolated structure when the lower structure is sufficiently rigid.

4.2. Time-History Analysis. To further confirm the validity of the obtained analytical results, a series of time history analyses subjected to earthquake excitations were carried out for the three cases. Three real earthquake records were selected as input ground motions: the EW component of El Centro 1940, the NS component of Taft 1952, and the NS component of Hachinohe 1968. The magnification factor M, defined as ratios of maximum acceleration responses to peak ground acceleration (PGA), is shown in Figures 14–16.

As shown in Figures 14–16, for Case 1, located in the coupling region A, the magnification factor M decreases for the upper and isolated masses and increases for the lower mass as the frequency ratio ε_{ls} increases. For Case 2, located in the intersection of regions A and C, the increase of ε_{us}
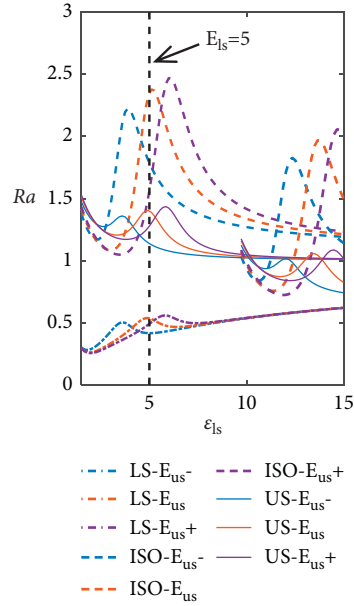
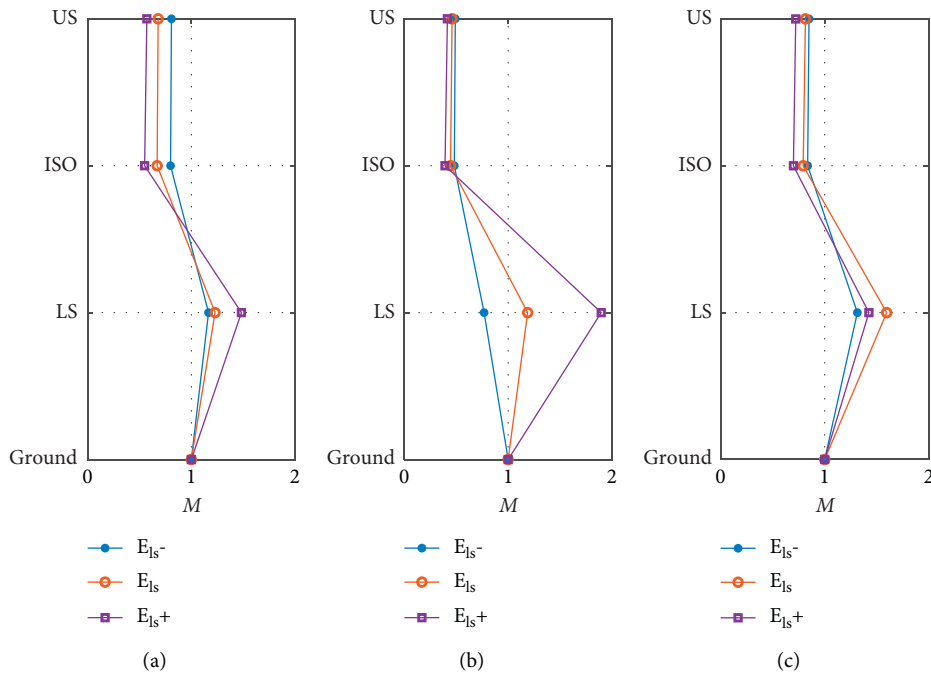FIGURE 13: RMS ratios Ra with various ε_{ls} (Case 3).

FIGURE 14: The magnification factor M for Case 1: (a) El Centro-EW, (b) Taft-NS, and (c) Hachinohe-NS.

above the peak line in region C leads to an increase of the magnification factor M of the upper and isolated masses. For Case 3, located in the coupling region C, the maximum magnification factor M for all masses is obtained when $\varepsilon_{ls} = E_{us}$, which indicates that either increasing or decreasing the stiffness of the lower structure here can reduce the structural response. These results are consistent with those obtained from the frequency domain analysis.
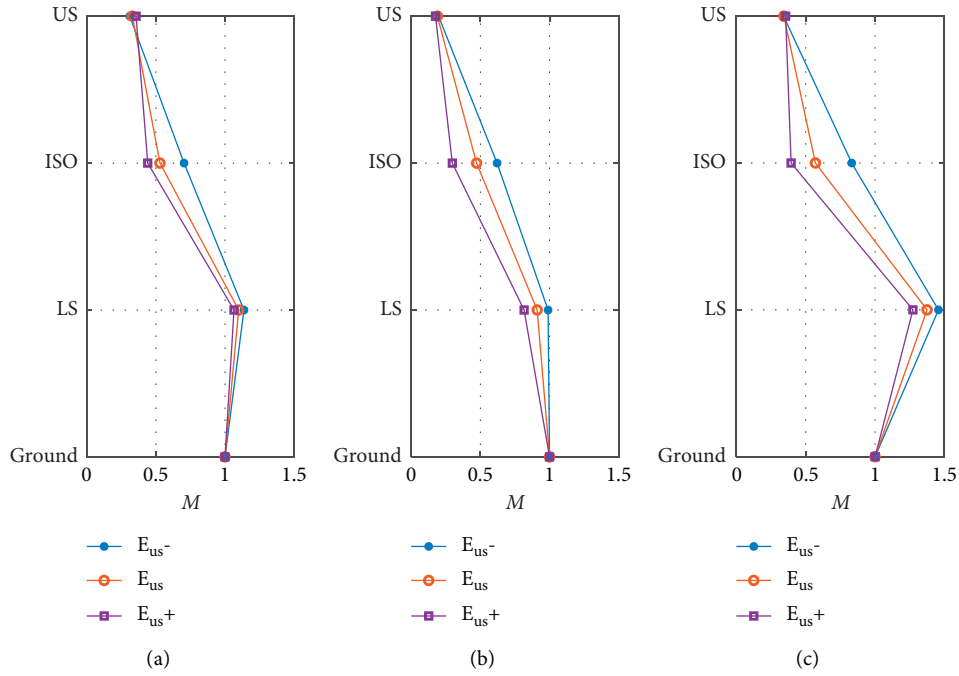
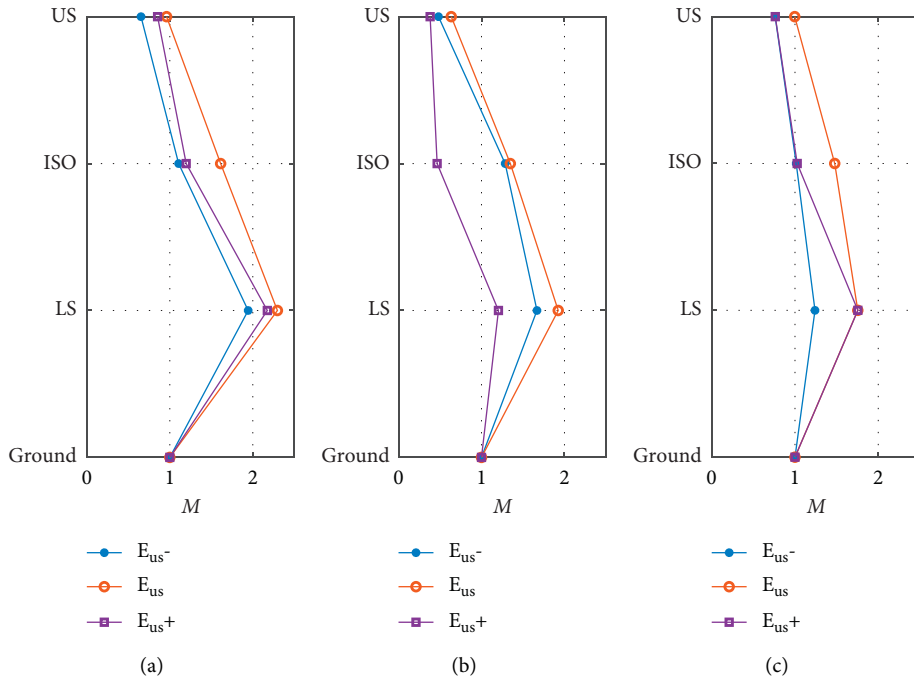FIGURE 15: The magnification factor M for Case 2: (a) El Centro-EW, (b) Taft-NS, and (c) Hachinohe-NS.

FIGURE 16: The magnification factor M for Case 3: (a) El Centro-EW, (b) Taft-NS, and (c) Hachinohe-NS.

5. Conclusion

Based on random vibration analysis, this study proposed a method to evaluate the coupling effect of the MSI systems. Explicit dynamic response formulas are derived for the MSI systems (represented by the F model), the base isolation systems (represented by the 2DOF model), and the fixed-base systems (represented by the S-DOF model) under white-noise excitation. The RMS ratio of the shear force coefficient of the upper isolation system is adopted as the performance indicator to evaluate the coupling amplification effect of the MSI system. In addition, the coupling effect region corresponding to a certain threshold can be obtained with different structural parameters. Finally, the time-

domain analysis was performed to verify the reliability of the results obtained from the frequency domain analysis. Some conclusions can be drawn as follows:

(1) The frequency ratios ε_{ls} and ε_{us} and mass ratios r_1 and r_2 have a significant effect on the dynamic characteristics and dynamic response of the MSI systems. The mass ratio r_1 mainly affects the distribution of contribution between the first and higher modes, while the mass ratio r_2 affects the distribution of contribution between the second and the third modes.

(2) The coupling effect between adjacent modes amplifies the seismic response of the upper isolation system compared to the corresponding base isolation system. In contrast, the coupling effect effectively reduces the seismic response of the lower structure compared to that of the fixed-base system.

(3) In general, the region where the coupling effect should be considered can be divided into two parts, regions A and C, according to the thresholds of the performance indicator. As mass ratios r_1 increases, region C shrinks and eventually disappears, indicating that the coupling amplification effect in this region is negligible under certain conditions.

(4) In region A, where the amplification effect is caused by modal coupling between the first and second

modes, the effect of frequency ratio ε_{ls} is more significant than frequency ratio ε_{us}. The performance indicator Ra_{ui} decreases rapidly with increasing ε_{ls} and remains essentially constant with increasing ε_{us}. In region C, where the amplification effect is caused by modal coupling between second and third modes, there is a peak line on which the maximum of indicator Ra_{ui} can be obtained. The peak line in region C is approximately parallel to the boundary line of the region. The results show that the seismic response of the upper isolation system can be reduced by slightly adjusting the frequency ratios ε_{ls} and ε_{us} according to the characteristics of different regions.

(5) The effect of the damping ratio on the amplification effect varies in different regions and needs to be determined according to the frequency ratios ε_{ls} and ε_{us} and mass ratios r_1 and r_2.

The proposed approach does not require detailed dynamic simulations of the system components and can be applied in the preliminary design of the MSI structures.

Appendix

$$\sigma^2 = \int_{-\infty}^{\infty} |H(\omega)|^2 d\omega = \omega_{iso} \cdot \int_{-\infty}^{\infty} \frac{\Xi_m(\varepsilon)}{\Lambda_m(i\varepsilon)\Lambda_m(-i\varepsilon)} d\varepsilon = \omega_{iso} \cdot \frac{AA}{BB},$$

$$\Xi_m(\varepsilon) = B_{m-1}\varepsilon^{2m-2} + B_{m-2}\varepsilon^{2m-4} + \cdots + B_0,$$

$$\Lambda_m(i\varepsilon) = A_m(i\varepsilon)^m + A_{m-1}(i\varepsilon)^{m-1} + \cdots + A_0,$$

(A.1)

where

$$\begin{aligned} AA = &-A_0^3 A_5^3 - 3A_0^2 A_1 A_3 A_5 A_6 + 2A_0^2 A_1 A_4 A_5^2 + A_0^2 A_2 A_3 A_5^2 + A_0^2 A_3^3 A_6 - A_0^2 A_3^2 A_4 A_5 - A_0 A_1^3 A_6^2 \\ &+ 2A_0 A_1^2 A_2 A_5 A_6 + A_0 A_1^2 A_3 A_4 A_6 - A_0 A_1^2 A_4^2 A_5 - A_0 A_1 A_2^2 A_5^2 - A_0 A_1 A_2 A_3^2 A_6 + A_0 A_1 A_2 A_3 A_4 A_5, \\ BB = &-B_5 A_0^3 A_5^2 - B_5 A_0^2 A_1 A_3 A_6 + 2B_5 A_0^2 A_1 A_4 A_5 + B_3 A_0^2 A_1 A_5 A_6 + B_5 A_0^2 A_2 A_3 A_5 - B_5 A_0^2 A_3^2 A_4 \\ &- B_3 A_0^2 A_3^2 A_6 - B_1 A_0^2 A_3 A_5 A_6 + B_5 A_0 A_1^2 A_2 A_6 - B_5 A_0 A_1^2 A_4^2 - B_3 A_0 A_1^2 A_4 A_6 - B_1 A_0 A_1^2 A_6^2 \\ &- B_5 A_0 A_1 A_2^2 A_5 + B_5 A_0 A_1 A_2 A_3 A_4 + B_3 A_0 A_1 A_2 A_3 A_6 + B_1 A_0 A_1 A_2 A_5 A_6. \end{aligned}$$

(A.2)

Data Availability

The data used to support the findings of this study are included within the article.

Conflicts of Interest

The authors declare that there are no conflicts of interest regarding the publication of this paper.

Acknowledgments

References

[1] M. Ziyaeifar and H. Noguchi, "Partial mass isolation in tall buildings," *Earthquake Engineering & Structural Dynamics*, vol. 27, no. 1, pp. 49–65, 1998.

[2] K. Ogura, M. Takayama, O. Tsujita, Y. Kimura, and A. Wada, "Seismic response of mid-story isolated b," *Journal of Structural and Construction Engineering (Transactions of AIJ)*, vol. 64, no. 516, pp. 99–104, 1999.

[3] T. Koh, Kobayashi, and M. Kobayashi, *Vibratory Characteristics and Earthquake Response of Mid-Story Isolated Buildings*, Memoirs of the Institute of Sciences and Technology, Meiji University, vol. 39, no. 12, , pp. 97–114, Tokyo, Japan, 2000.

[4] A. Keivan, R. Zhang, D. Keivan, B. M. Phillips, M. Ikenaga, and K. Ikago, "Rate-independent linear damping for the improved seismic performance of inter-story isolated structures," *Journal of Earthquake Engineering*, vol. 2020, pp. 1–24, 2020.

[5] K. Ogura, I. Kawabata, T. Komuro, K. Soya, and T. Terashima, "Seismic response characteristics of high-rise buildings with base isolation system," *AIJ Journal of Technology and Design*, vol. 3, no. 5, pp. 47–51, 1997.

[6] S. Kawamura, R. Sugisaki, K. Ogura, and S. Maezawa, "Seismic isolation retrofit in Japan," in *Proceedings of the 12th World Conference of Earthquake Engineering*, vol. 2523, Upper Hutt, Auckland, February 2000.

[7] K. Murakami, H. Kitamura, H. Ozaki, and T. Teramoto, "Design and Analysis of a Building with the Middle-story Isolation Structural System," in *Proceedings of the 12th World Conference of Earthquake Engineering*, vol. 857, Auckland, New Zealand, February 2000.

[8] T. Sueoka, S. Torii, and Y. Tsuneki, "The application of response control design using middle-story isolation system to high-rise building," in *Proceedings of the 13th World Conference on Earthquake Engineering*, vol. 3457, Vancouver, Canada, August 2004.

[9] Y. Tsuneki, S. Torii, K. Murakami, and T. Sueoka, "Middle-story isolated structural system of high-rise building," in *Proceedings of 14th World Conference on Earthquake Engineering*, Beijing, China, October 2008.

[10] K. Okada and S. Yoshida, "Structural design of Nakanoshima festival tower," *International Journal of High-Rise Buildings*, vol. 3, no. 3, pp. 173–183, 2014.

[11] D. Nakamizo and Y. Koitabashi, "Structural design of mid-story isolated high-rise building-Roppongi Grand Tower," *International Journal of High-Rise Buildings*, vol. 7, no. 3, pp. 233–242, 2018.

[12] J. L. Xie and F. L. Zhou, "Test, research, and application of the top isolation-TMD for multi-story buildings," *World Information on Earthquake Engineering*, vol. 14, no. 12, pp. 22–30, 1998.

[13] M. Tasaka, N. Mori, H. Yamamoto, and K. Murakami, "Applying Seismic Isolation to Buildings in Japan—retrofitting and Middle-story Isolation," in *Proceedings of the Structures Congress 2008: 18th Analysis and Computation Specialty Conference*, April 2008.

[14] M. D'Amato, R. Gigliotti, and R. Laguardia, "Seismic isolation for protecting historical buildings: a case study," *Frontiers in Built Environment*, vol. 5, no. 87, 2019.

[15] D. D. Tan, Z. Q. Lu, D. H. Gu, H. Ding, and L. Q Chen, "A ring vibration isolator enhanced by a nonlinear energy sink," *Journal of Sound and Vibration*, vol. 508, no. 1-3, Article ID 116201, 2021.

[16] A. Dutta, J. F. Sumnicht, R. L. Mayes, R. O Hamburger, and A. Citipitioglu, "An Innovative Application of Base Isolation Technology," in *Proceedings of the Structures Congress 2008: 18th Analysis and Computation Specialty Conference*, ASCE Library, Vancouver, Canada, April 2008.

[17] H.-S. Kim and J.-W. Kang, "Optimal design of smart mid-story isolated control system for a high-rise building," *International Journal of Steel Structures*, vol. 19, no. 6, pp. 1988–1995, 2019.

[18] R. Zhang, M. Wu, F. Zhou, and J. Jiang, "Research on mid-story isolation of structure using inerter isolation system," *World Earthquake Engineering*, vol. 36, no. 4, pp. 8–16, 2020.

[19] A. Saha and S. K. Mishra, "Seismic response mitigation of structure by negative stiffness devices via mid-story weakening," *Lecture Notes in Mechanical Engineering*, Advances in Structural Vibration, Springer, vol. 2021, pp. 223–231, Berlin, Germany, 2021.

[20] J. Bian and X. Jing, "Analysis and design of a novel and compact X-structured vibration isolation mount (X-Mount) with wider quasi-zero-stiffness range," *Nonlinear Dynamics*, vol. 101, no. 4, pp. 2195–2222, 2020.

[21] H. Dai, X. Jing, Y. Wang, X. Yue, and J. Yuan, "Post-capture vibration suppression of spacecraft via a bio-inspired isolation system," *Mechanical Systems and Signal Processing*, vol. 105, pp. 214–240, 2018.

[22] G. Gatti, "Effect of parameters on the design of a suspension system with four oblique springs," *Shock and Vibration*, vol. 2021, Article ID 5556088, 16 pages, 2021.

[23] G. Gatti, "A K-shaped spring configuration to boost elastic potential energy," *Smart Materials and Structures*, vol. 28, no. 7, 2019.

[24] A. D. Shaw, G. Gatti, P. J. P. Gonçalves, and B. Tang, "Design and test of an adjustable quasi-zero stiffness device and its use to suspend masses on a multi-modal structure," *Mechanical Systems and Signal Processing*, vol. 152, Article ID 107354, 2021.

[25] N. Hirotani and I. Hata, "A study on building mass damper system using mid-story isolated system," *Journal of Structural and Construction Engineering (Transactions of AIJ)*, vol. 83, no. 753, pp. 1573–1582, 2018.

[26] Y. Terazawa, W. Sano, and T. Takeuchi, "Design method of seismically isolated structures based on generalized response spectrum analysis," *Journal of Structural and Construction Engineering (Transactions of AIJ)*, vol. 85, no. 775, pp. 1187–1197, 2020.

[27] Y. Tomiyoshi, M. Takahashi, S. Kotsuki, H. Kambara, and A. Fukukita, "Design of an active mass damper to simultaneously mitigate seismic acceleration in superstructures and substructures of a mid-story isolation building," *The Proceedings of the International Conference on Motion and Vibration Control*, vol. 2020, Article ID 10103, 2020.

[28] Z. Q. Lu, D. H. Gu, H. Ding, L. Walter, and C. Li-Qun, "Nonlinear vibration isolation via a circular ring," *Mechanical Systems and Signal Processing*, vol. 136, Article ID 106490, 2019.

[29] Z.-Q. Lu, D. Wu, H. Ding, and L.-Q. Chen, "Vibration isolation and energy harvesting integrated in a Stewart platform with high static and low dynamic stiffness," *Applied Mathematical Modelling*, vol. 89, pp. 249–267, 2021.

[30] M. Kobayashi, Y. Izawa, and T. Koh, "The prediction method OF earthquake responses ON mid-story isolated system considering modal coupling effect: earthquake response prediction and aseismic performance of mid-story isolated system Part 2," *Journal of Structural and Construction Engineering (Transactions of AIJ)*, vol. 68, no. 572, pp. 73–80, 2003.

[31] M. Kobayashi and T. Koh, "Modal coupling effects of mid-story isolated buildings," in *Proceedings of the 14th World conference on earthquake engineering*, vol. 2008, Beijing, China, May 2008.

[32] S.-J. Wang, K.-C. Chang, J.-S. Hwang, and B.-H. Lee, "Simplified analysis of mid-story seismically isolated buildings," *Earthquake Engineering & Structural Dynamics*, vol. 40, no. 2, pp. 119–133, 2011.

[33] S.-J. Wang, K.-C. Chang, J.-S. Hwang, J.-Y. Hsiao, B.-H. Lee, and Y.-C. Hung, "Dynamic behavior of a building structure tested with base and mid-story isolation systems," *Engineering Structures*, vol. 42, pp. 420–433, 2012.

[34] Y. Ikeda, "Fundamental equation based on pole allocation for interstory seismic isolation of buildings," *Structural Control and Health Monitoring*, vol. 28, no. 3, 2021.

[35] D. Faiella and E. Mele, "Vibration characteristics and higher mode coupling in intermediate isolation systems (IIS): a parametric analysis," *Bulletin of Earthquake Engineering*, vol. 17, no. 7, pp. 4347–4387, 2019.

[36] D. Faiella and E. Mele, "Insights into inter-story isolation design through the analysis of two case studies," *Engineering Structures*, vol. 215, Article ID 110660, 2020.

[37] J. M. Kelly, *Earthquake-resistant Design with Rubber*, pp. 43–59, Springer, Berlin, Germany, 1993.

[38] J. B. Roberts and P. D. Spanos, *Random Vibration and Statistical Linearization*, pp. 382–386, Courier Corporation, Chelmsford, MA, USA, 2003.